EMPIRICAL NLTE ANALYSES OF SOLAR SPECTRAL LINES

II: *The Formation of the Ba II λ4554 Resonance Line*

ROBERT J. RUTTEN

Sterrewacht 'Sonnenborgh', the Astronomical Institute, Utrecht, The Netherlands

(Received 10 August, 1977)

Abstract. The center-to-limb behaviour of the Ba II λ4554 resonance line is analyzed together with data from the extreme limb, flash intensities and profiles of other Ba II lines. An empirical NLTE method is employed in which the observed profiles are compared with synthesized profiles based on a standard one-dimensional model atmosphere, with the line source function, the barium abundance, the collisional damping and the atmospheric turbulence as free parameters.

The line profiles from the extreme limb furnish considerable constraints on the formation of Ba II λ4554. Its wings reverse into emission well inside the solar limb, a phenomenon which cannot be explained by any frequency-independent line source function. Accounting for effects of partially coherent scattering in the line source function is a necessary and adequate step to reproduce the observations both over the disk and near the limb. The form of the empirically derived frequency-dependent line source function is discussed.

Results are given for various parameters (*gf*-values, solar barium abundance and isotope ratios, collisional damping, microturbulence and macroturbulence).

The λ4554 profile of disk center shows a depression in its blue wing resembling asymetries found in various stellar spectral lines.

1. Introduction

This paper presents the first attempt to derive the source function and other formation parameters of a solar spectral line from observations of the *complete* center-to-limb behaviour of its profile, including profiles from the extreme limb of the Sun. Such profiles were obtained for the Mg I λ4571 intercombination line and for the Ba II λ4554 resonance line at the 1970 solar eclipse (Rutten, 1977); the Ba II λ4554 line is analyzed here.

The Ba II spectrum is of interest, firstly because barium is a 'magic neutron number'-step in the formation of the heavy elements and shows strengthened lines in barium star spectra (Bidelman and Keenan, 1951; Burbidge and Burbidge, 1957; Warner, 1965).

Secondly, the large atomic weight of barium (137.4 in the chemical scale) makes its lines less sensitive to thermal broadening: their thermal Doppler widths are only half that of calcium. The barium lines are therefore good indicators of non-thermal broadening by systematic motions, turbulence and collisions. Indeed, the supergranulation velocity pattern is best seen in λ4554 (Noyes, 1967).

Thirdly, the solar Ba II spectrum offers a test of spectroscopic diagnostic techniques. It contains the only unblended resonance line of the dominant ionization

Solar Physics **56** (1978) 237–262.

stage of an element in the visible region other than Ca II H and K. Ba II λ4554 is quite similar to Ca II K in atomic origin, but of course far weaker.

Previous analyses of the Ba II lines in the photospheric spectrum were largely devoted to the determination of the barium abundance (Goldberg *et al.*, 1960; Lambert and Warner, 1968; Holweger and Müller, 1974). The most extensive of these is the recent analysis of the Ba II lines at disk center by Holweger and Müller, who assumed LTE and an updated version of Holweger's (1967) model atmosphere. Tandberg-Hanssen (1964) and Tandberg-Hanssen and Smythe (1970) analyzed the NLTE formation of the two Ba II resonance lines high in the chromosphere from integrated line strengths in flash spectra which show unexpected strength ratios of the two lines.

In the present analysis the usual assumptions are made that the solar atmosphere consists of homogeneous parallel layers, and that the averaged effects of non-thermal motions and of inhomogeneities can be described with the microturbulent and macroturbulent limits of uncorrelated, gaussian-distributed velocities. The empirical NLTE approach of Wijbenga and Zwaan (1972; the first paper in this series) is taken. As in the classical LTE method the emergent line profiles are synthesized by direct integration of the source function. The line source function, however, is not fixed by the electron temperature but specified with adaptable height-dependent NLTE-departure coefficients, to be determined by trial-and-error fitting. The other line formation parameters are likewise derived empirically.

As in any interpretation of solar spectral lines, a problem is posed by the large number of parameters that enter. The remedy usually taken is to restrict the number of parameters by simplifying assumptions, such as the validity of LTE, of complete redistribution, of model atom calculations, or the neglect of the height dependence and anisotropy of the turbulence parameters. In the empirical method used here no such a priori assumptions are made. It is then essential to calculate profiles for many different parameter sets and so obtain the 'response function' of the line for each parameter. Even then, as in any other approach, a good fit does not guarantee uniqueness. The advantage of the empirical method is that no uncertainties are hidden – in fact the uniqueness problem is clearly evident.

As discussed by Wijbenga and Zwaan (1972), redundancy may be obtained by analyzing complete spectra with connecting transitions, which are observed not only over the disk but also from the limb. Data from the extreme limb extend the normal center-to-limb variation with a range in which large changes occur in line formation. Such data are readily incorporated in the empirical fitting approach.

The additional constraints furnished by the profiles of λ4554 from the extreme limb play indeed an important part in this analysis. The wings of the line change into emission relative to the local continuum at ≈ 1500 km inside the limb. Surprisingly, these features appeared to be difficult to explain, turning the analysis into a test of the spectroscopic method itself.

The analysis is presented in order of increasingly complex line formation, starting with the classical LTE approach. In Section 2 the empirical method and the atomic

data are described. In Section 3 the observations are reviewed. Section 4 presents line synthesis results for LTE and various degrees of NLTE assuming complete frequency redistribution. In section 5 a wavelength-dependent line source function is introduced for λ4554, which is discussed in Section 6 together with other results. A more detailed account may be found in Rutten (1976).

2. Formulation

2.1. Line synthesis program

A spectral line synthesis program was used which applies curved-layer geometry to calculate profiles near or above the limb as well as on the disk (Rutten, 1976). Only a brief description is given here. The program calculates emergent line profiles from a one-dimensional atmospheric model by evaluating

$$I_\lambda(h_0) = \int_{-\infty}^{\infty} \varepsilon_\lambda(h) \exp\left[- \int_{-\infty}^{y} \kappa_\lambda(h)\, dy' \right] dy, \tag{1}$$

where I_λ is the emergent monochromatic intensity along the line of sight defined by the viewing angle θ or the projected height above the limb h_0, y and y' are geometrical depth variables along the line of sight, and h measures the radial height above the solar limb. The limb ($h = 0$) is defined as usual in eclipse analyses as the location where the continuum at 5000 Å has a total *tangential* optical depth of unity; the height scales of the model atmospheres are shifted so that this definition applies. The height $h = 0$ is then close to the inflection point in the continuum decline. The parameter ε_λ is the total emission coefficient per cm^3, κ_λ is the total absorption coefficient per cm^3. These are evaluated for specified wavelengths covering the profile at every height point of the model atmosphere. The continuous absorption and emission processes are assumed to be in LTE; Thomson and Rayleigh scattering are included. The line absorption and emission coefficients are calculated assuming complete redistribution, and taking into account the neutral, first and second barium ionization stages, hyperfine structure, temperature-dependent partition functions, stimulated emission and various collisional broadening processes. Further details may be found in Rutten (1976), and also in Landi Degl' Innocenti (1976).

2.2. Atomic data

The Ba II lines used are specified in Table I and Figure 1. The empirical *oscillator strengths* (Table I) have been taken from the compilation of the Ba II spectrum by Miles and Wiese (1969). The theoretical oscillator strengths are respectively from the list of Kurucz and Peytremann (1975) and from calculations with the scaled Thomas-Fermi program of Van Rensbergen (1970). In all calculations the experimental values were used.

TABLE I

Identifications and atomic data for the Ba II lines used in this investigation. Explanation in text

Mult. No.	λ (Å)	Transition	W_λ center (mÅ)	Lower E.P. (eV)	log *gf* obs.	log *gf* KP	log *gf* vR	γ_{RAD} (s^{-1})	C_6	α_6	β_6	HFS components	
												Δλ (mÅ)	Rel. int.
												−0.17	0.821
1	4554.04	$6S_{1/2}-6P_{3/2}$	188	0.000	0.17	0.19	0.24	2.9×10^{8}	7.1×10^{-33}	4.6×10^{-10}	0.407	+17.57	0.112
												−34.08	0.067
2	5853.69	$5D_{3/2}-6P_{3/2}$	63	0.604	−1.00	−1.16	−1.04	2.9×10^{8}	1.4×10^{-32}	6.8×10^{-10}	0.356		
2	6141.72	$5D_{5/2}-6P_{3/2}$	120	0.704	−0.08	−0.16	−0.09	2.9×10^{8}	1.4×10^{-32}	6.8×10^{-10}	0.356		
												0.00	0.821
												−4.12	0.034
2	6496.91	$5D_{3/2}-6P_{1/2}$	100	0.604	−0.38	−0.47	−0.36	2.9×10^{8}	1.3×10^{-32}	6.6×10^{-10}	0.356	−3.74	0.078
												+8.92	0.067
4	4130.66	$6P_{3/2}-6D_{5/2}$	≈35	2.721	0.68	0.55	0.56	8.5×10^{8}	2.8×10^{-32}	9.9×10^{-10}	0.361		

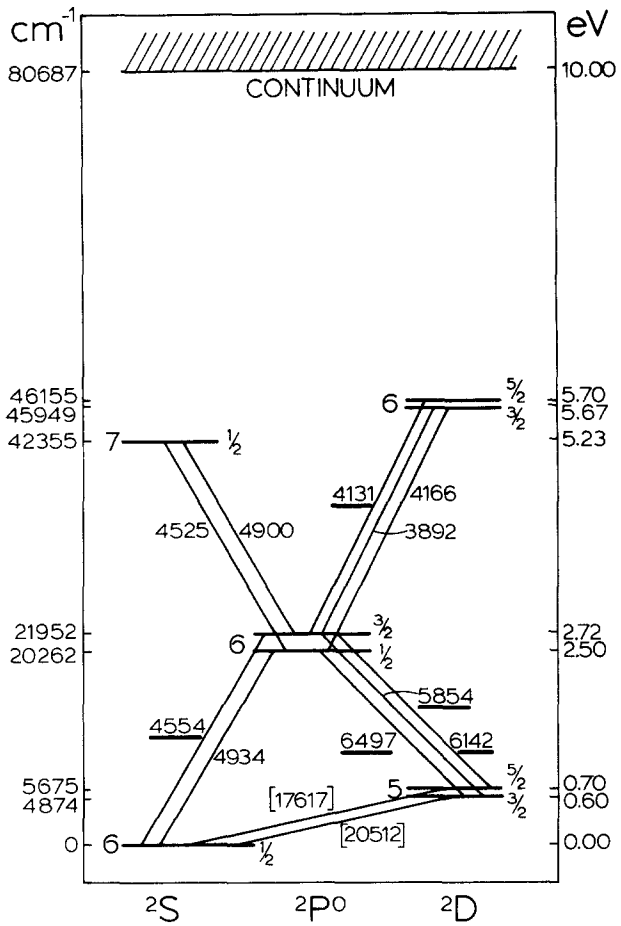

Fig. 1. Energy level diagram for Ba II. The wavelengths of the analyzed transitions are underlined.

The *radiative damping constants* in Table I are the sums of all contributing transition probabilities given by Miles and Wiese (1969), neglecting absorption and stimulated emission. The *collisional damping constants* C_6 specify the Van der Waals broadening by neutral H and He atoms, using the Bates-Damgaard approximation for the mean square atomic radii (Unsöld, 1955, expr. 82.48, 84.41ff.). The coefficients α_6 and β_6 define power-law fits to the newer damping values of Deridder and Van Rensbergen (1974, 1976):

$$\gamma_6 = \alpha_6 T_e^{\beta_6} N_H, \tag{2}$$

where γ is the full half-width of the damping profile in angular frequency. These values, kindly calculated by Deridder, are based on a theory in which the Van der Waals potential is replaced by a Smirnov-Roueff potential for the close interactions (Van Rensbergen *et al.*, 1975). The other collisional broadening processes (Stark broadening, quadrupole broadening) are negligible, as are the predicted collisional

line shifts (Rutten, 1976). In view of the uncertainty in the collisional damping its value was treated as a free parameter by introducing the usual arbitrary multiplication factor.

Hyperfine structure (HFS) must be included for λ4554 (Holweger and Müller, 1974). The most recent tabulation of experimental data on HFS in Ba II lines is that of Brix and Kopfermann (1952). Table II specifies their values of the fine structure constant A, and also theoretical values that were kindly calculated by Deridder with the Goudsmit-Fermi-Segré formula for hydrogen-like spectra, including the relativistic and alkali corrections (Kopfermann, 1956, expr. 26.24ff). The agreement with the measured values is excellent. The splitting patterns of all lines of Table I were determined from the calculated values following Candler (1964). The isotope shifts and terrestrial abundance ratios were taken from Brix and Kopfermann (1952). The splitting pattern of the λ4554 line has appreciable width (Figure 2). Fortunately, the 3-component simplification given in Table I is

TABLE II

Measured (A_m) and computed (A_c) hyperfine structure constants in 10^{-3} cm^{-1} for various Ba II levels

	Ba 135		Ba 137	
Term	A_m	A_c	A_m	A_c
$6s\ ^2S_{1/2}$	121.5	121.8	135.5	135.96
$5d\ ^2D_{3/2}$	—	3.56	—	3.97
$5d\ ^2D_{5/2}$	—	1.49	—	1.66
$6p\ ^2P^0_{1/2}$	20.8	21.7	23.2	24.2
$6p\ ^2P^0_{3/2}$	4	3.47	5	3.88
$6d\ ^2D_{5/2}$	≈0	0.38	≈0	0.43

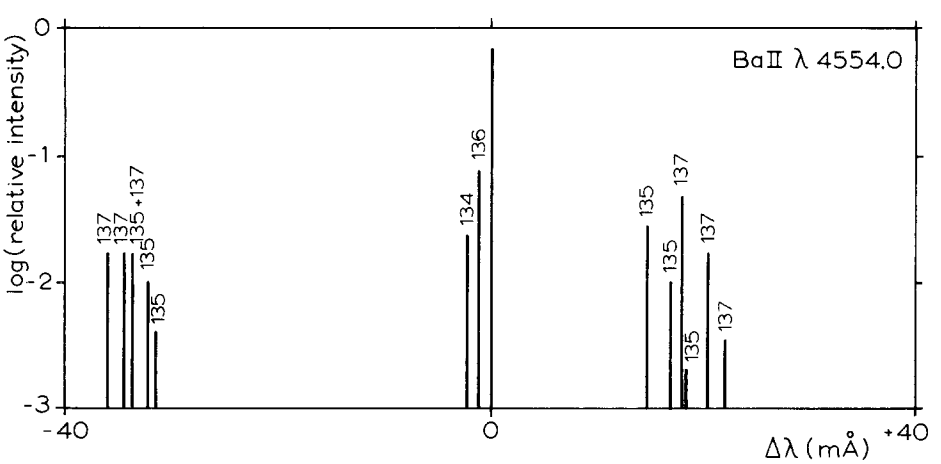

Fig. 2. Splitting pattern of the λ4554 line for terrestrial isotope ratios. The various components are identified by their isotope numbers; the central component is chiefly due to Ba 138.

sufficiently precise. The other Ba II lines have less extensive HFS patterns. The total widths of the patterns of λ5854, λ6142, and λ4131 are respectively 10 mÅ, 14 mÅ and 5 mÅ, and were neglected. The 23 mÅ wide pattern of the λ6497 line was approximated by the four components listed in Table I.

3. Observations

3.1. Disk data

High-quality profiles of the five Ba II lines were used, each observed at five positions on the solar disk. They were obtained with the McMath Solar Telescope and Vacuum Spectrograph at Kitt Peak National Observatory. Except for the λ4131 line, these data were collected by L. Testerman of KPNO as part of the 'Fast Center-Limb Survey'. They were reduced by H. Nieuwenhuijzen, who applied the standard KPNO restoration procedures (Evans and Testerman, 1975), and who also obtained similar observations of the λ4131 line. The rms-error in these measurements is about 0.2% of the continuous intensity. Comparable observations of the λ4554 line, obtained with the spectrometer at the Jungfraujoch Scientific Station, were kindly provided by L. Neven. They agree with the KPNO data to within 0.5% of the continuous intensity. Since the fitting with the computed profiles was not pursued to better resolution than 1% of the continuous intensity, the quality of these profiles is quite sufficient.

3.2. Limb data

The Utrecht expedition to the 1970 eclipse obtained profiles of the λ4554 resonance line from the extreme limb of the Sun (Houtgast *et al.*, 1976; Rutten, 1977). The unusual use of a slit ensured sufficient spectral resolution for the derivation of detailed line profiles. The height calibration of the spectrograms, based on a slit-jaw film, is better than 100 km. An absolute intensity calibration was not obtained.

The eclipse profiles of λ4554 are divided into two groups (Rutten, 1977). The first covers the range $1/\mu = 4 - 22$, where μ is the cosine of the viewing angle of the Moon's limb at mid-exposure. These profiles are still so far from the limb ($1/\mu = 22$ corresponds to $h_0 = -720$ km, where h_0 is the projected height above the limb), that the uncertainty in the definition and location of the observed limb is not important and that the advance of the lunar limb during the exposures may be neglected. Because the seeing was poor during the observations, the mid-exposure lines of sight represent lower cutoffs of an integration over the height of the yet uncovered atmosphere. The second group consists of three profiles at and above the limb (Figure 11). These profiles have not been used in the analysis because of their uncertainties; they serve as a test afterwards.

In Figure 3 eclipse profiles and KPNO profiles are compared for the region of overlap. The agreement is good except for the far wings which have larger intensity

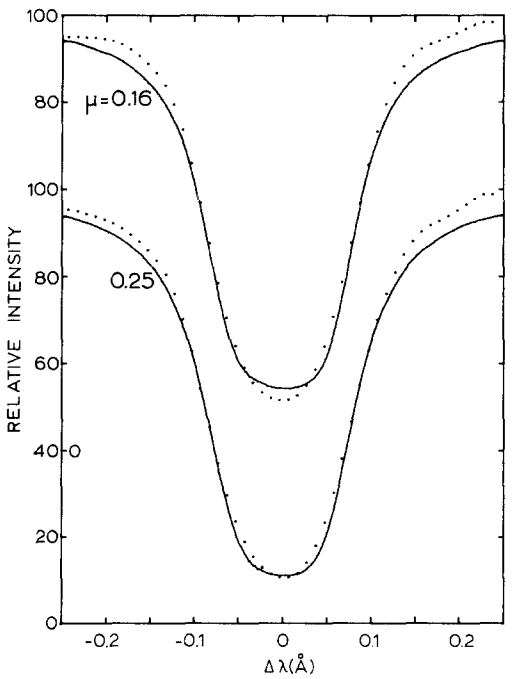

Fig. 3. A comparison of Kitt Peak observations (*lines*) and eclipse data (*dots*) for different values of $1/\mu$ for which they overlap (μ is cosine of the viewing angle). *Ordinate*: relative intensity (continuum = 100%), with a vertical offset of 40% for the top profiles. *Abscissa*: wavelength separation from line center.

in the eclipse profiles. This difference is probably due to systematic errors in the photometric calibration that result from local over-exposure around λ4554. Fortunately this over-exposure decreases towards the limb (Rutten, 1977). The eclipse profiles show less boxy cores than the KPNO profiles due to their lower spectral resolution.

3.3. Asymmetries

The λ4554 resonance line shows asymmetry in its core and in the shoulders of its wings. At disk center the line core has a boxy, asymmetrical shape caused by the hyperfine splitting of the odd barium isotopes. The asymmetry in the wings at −0.1 Å from line center is more puzzling. It is not immediately apparent because there is no clearly defined line center due to the HFS splitting. The asymmetry appears during profile fitting: the synthesized profiles are higher at the blue shoulder than the observed profile. The depression is largest at disk center (Figure 6a). I describe it as a discrepancy of the blue wing rather than of the red (or a shift of the line core with respect to the wings, cf. Magnan and Pecker, 1974) because it is possible to fit the line core, red wing and far blue wing simultaneously, while fits to the blue shoulder consistently destroy fits of the core together with the near and far

red wing. A 'Minnaert plot' (Figure 4) illustrates this (Minnaert, 1935; Unsöld, 1955, p. 245). From trial calculations (Rutten, 1976) it was concluded that this asymmetry is not due to errors in the continuum determination, to a different barium isotope ratio or to the presence of a single blend. It is caused either by a number of small, deeply formed blends or, more likely, by effects of moving inhomogeneities. Similar blue-wing depressions have been reported for some stellar spectra (Smith and Parsons, 1975, 1976). In the following, the fitting procedure was concentrated on the line core, the whole red wing and the far blue wing.

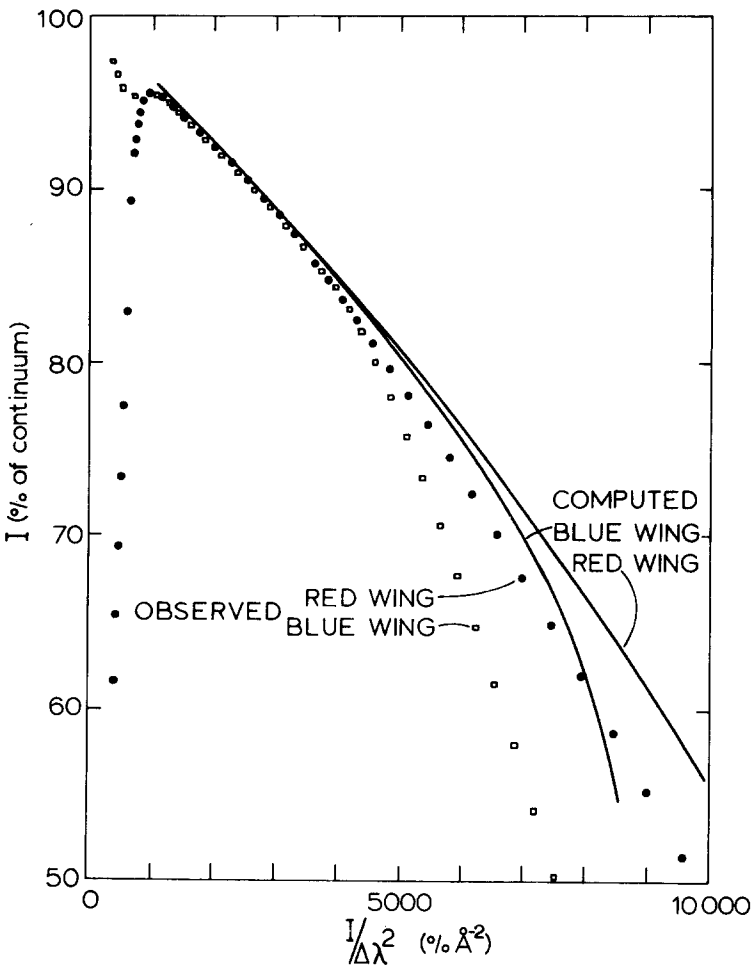

Fig. 4. A Minnaert plot for the λ4554 line at disk center. The computed profile is for the best-fit model (Section 5). *Ordinate*: relative intensity (continuum = 100%). *Abscissa*: relative intensity divided by squared wavelength separation from line center. The wild behaviour on the left is caused by far away blends. The far wings of the computed and observed profiles agree well, showing that the observed line core and damping wings define the same line-center wavelength. Their extrapolation intersects the ordinate at 100%, confirming the continuum determination. The difference between the computed blue and red shoulders is due to hyperfine structure; the observed difference is appreciably larger.

4. Calculations Based on Complete Redistribution

4.1. LTE EVERYWHERE

It is impossible to reproduce the λ4554 profiles on the disk with LTE calculations for any model with a chromospheric temperature rise, because emission cores are then inevitable on the disk. Since these are not observed on the disk or at the limb, LTE calculations can only reproduce the observed profiles when less realistic electron temperature models are used that have no outward rise. This is the strategy of Holweger and Müller (1974), whose model decreases smoothly to 3900 K at 500 km above the limb. They find that the cores of the stronger Ba II lines (λ4554, λ6497, λ5854) for this model are too shallow at disk center, and conclude that this discrepancy confirms the presence of NLTE effects in high layers noticed for the Ba II lines in Holweger's 1967 study. Since the use of such a model for strong lines is in itself an implicit NLTE formulation, this is rather an understatement: the discrepancies show that the Ba II lines do not adhere to the average NLTE excitation temperature defined by their model above the temperature minimum.

Holweger and Müller varied only the collisional damping multiplication factor per line to fit the equivalent widths of all Ba II lines at disk center with a single abundance value ($A = N(\mathrm{Ba})/N(\mathrm{H}) = 1.3 \times 10^{-10}$). This procedure is the reverse of Holweger's 1967 analysis in which he varied the abundance for a given Van der Waals damping constant.

Variation of more parameters is needed to improve the fits of Holweger and Müller (1974) in the cores of the lines and to extend them to other positions on the disk (Rutten, 1976).

4.2. NLTE IN HIGH LAYERS ONLY

The next step is to use an atmospheric model with a chromospheric temperature rise and to admit departures from LTE above the temperature minimum, in accordance with the conclusions of Holweger and Müller (1974).

The continuum model of Vernazza *et al.* (1976, model M, henceforward called VAL) is used, shifted in height over 361 km in order to conform to the eclipse height scale. The ground state population of Ba II is assumed to be in LTE, so that the λ4554 line can be discussed in terms of its upper level departure coefficient only, i.e. its source function or excitation temperature. This is a good approximation in the photosphere where barium is exclusively in the first ionization stage: the ionization to Ba III occurs above ≈400 km, in layers that contribute only to the saturated λ4554 core. Here departures from LTE in the ionization equilibrium are probable, but they do not strongly influence the disk and limb profiles. (Barium has at 10 eV the lowest second ionization potential of all elements.)

Figure 6a shows a very good fit to the disk profiles of λ4554 that was obtained with the excitation temperature of Figure 5. The low minimum of the VAL model, here extended to larger heights, results in a good fit of the deep cores. The fit was

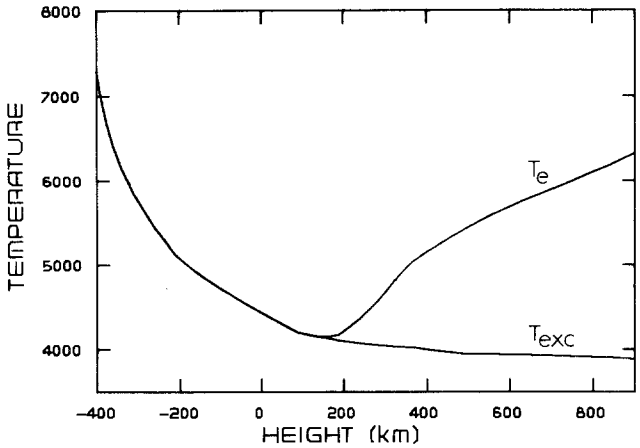

Fig. 5. CRD excitation temperature for the λ4554 line (best CRD fit, VAL atmosphere).

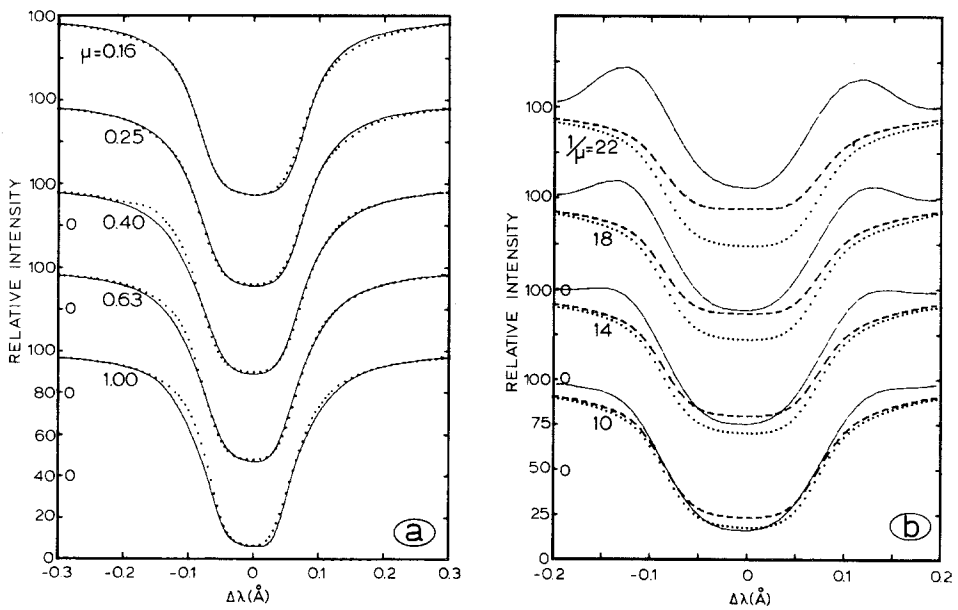

Fig. 6. Profiles of λ4554 for the best CRD fit. *Lines*: observed profiles. The computed profiles (*dots*) are for the VAL atmosphere, line source function defined by the excitation temperature of Figure 5, $A = 1.3 \times 10^{-10}$, $\gamma_6 = 1.85 \times$ Deridder-Van Rensbergen, microturbulence: 2 km s^{-1} below −400 km, decrease to 0.15 km s^{-1} at −150 km (vertical) and to 1.5 km s^{-1} at −150 km (horizontal), $v_{\text{macro}}^{\text{ver}} = 1.2$ km s^{-1}, $v_{\text{macro}}^{\text{hor}} = 1.7$ km s^{-1}. (a) Center-to-limb variation. *Ordinate*: specific intensity relative to the continuum = 100%, with vertical offsets of 40%. *Abscissa*: wavelength separation from line center. (b) Profiles near the limb. Labelling as for (a), vertical offsets 50%. *Dots*: computed without smearing by poor seeing. *Dashes*: computed with homogeneous blurring.

derived in successive approximations in which the excitation temperature, the abundance, the damping and the turbulence were varied. Details of this fit are not discussed here because solutions of this type are incompatible with the eclipse

observations discussed below. This fit serves only to demonstrate that a generalization of the Holweger-Müller procedure, applied to a more extended observational material, yields quite acceptable results – provided that only disk profiles are taken into account.

At about 1500 km *inside* the limb, the wings of the $\lambda 4554$ profile turn from absorption into emission. *Above* the limb such wing reversals are to be expected for lines with outwardly decreasing source functions as in Figure 5, when the line opacity at line center is still large enough to cause self-absorption, but not *on the disk*, where the continuous optical depth along the line of sight exceeds unity. Such emission must be accounted for by straylight or by source function effects. The straylight due to the bad seeing during the eclipse caused an averaging of the line profile over all uncovered solar atmosphere above the lunar limb, resulting in an apparent relative lowering of the observed continuum level. This blurring contributes therefore to the emission wings. Since the shape of the blurring function is not known, calculated profiles are given for the two extremes of no blurring at all and of 'homogeneous' blurring. In the latter case, the intensities are integrated outward without a weighting function, and scaled to the integrated continuous intensity, simulating slitless observations. This case is probably close to reality for $1/\mu < 10$ ($h_0 > -3600$ km), because the diameter of the seeing disk was about 5″ or 3600 km (Rutten, 1976; the projected slit width was only 0″.7).

Figure 6b shows profiles of $\lambda 4554$ at the limb together with profiles calculated with the fit of Figure 6a. The computed profiles show no emission wings at all, not even for homogeneous blurring. Figure 11b shows calculated profiles closer to and above the limb for the same fit. The unblurred profiles show self-absorption at the limb ($h_0 = 0$), but adding the line emission above the limb results in its disappearance and even in a slight emission core for $h_0 = -200$ km. The profiles are very much different, even in their gross shape, from the observed profiles from these regions (Figure 11a).

4.3. NLTE EXTENDED TO DEEP LAYERS

The failure of line source functions in reproducing the eclipse data when allowing departures from LTE only above the temperature minimum led to the examination of a variety of line source functions with an arbitrary height dependence. A large number of profiles were calculated for widely different sets of the various parameters. In spite of the large number of adjustable parameters, the observed profiles could not at all be fitted simultaneously with any line source function. This points to a deficiency in the basic assumptions of line formation. In the following section the introduction of a wavelength-dependent line source function will be presented as a remedy. In this section, the failure of the frequency-independent line source functions will be illustrated.

All calculations started with the definition of the run of the excitation temperature of the line with height by specifying a $\beta_u(h)-$ relation. The abundance and damping were varied to obtain fits in the cores and the wings of the disk profiles

respectively. The flanks of the profiles were then fitted by changing the turbulence parameters. A re-adjustment of the damping and abundance was often needed. Finally, profiles were calculated for the extreme limb and integrated using various blurring functions for comparison with the eclipse observations.

Three schematic types of line source function are represented by the excitation temperatures in Figure 7. Within the formulation of Section 2, the emission wings

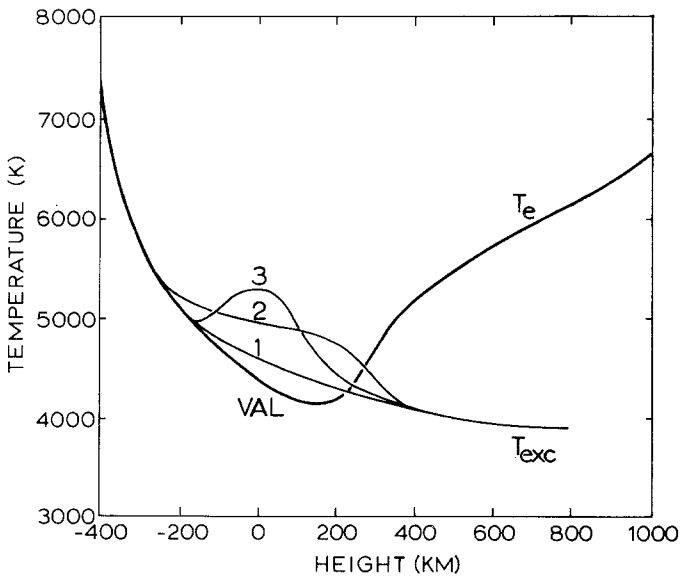

Fig. 7. Schematic diagram of formal excitation temperatures that define three types of line source functions for the λ4554 line.

near the limb must be caused by a rise of the line source function at their height of formation above the local Planck function at the height of formation of the continuum. The type 1 line source functions resemble the Holweger (1967) and Holweger-Müller (1974) excitation temperature models which, while decreasing monotonically outwards, run higher than the electron temperature of the current continuum models from −200 km onwards – a behaviour that still has to be explained (Athay, 1972, p. 183). However, higher excitation temperatures than these are needed, similar to Tanaka's (1971a, b) and Van Dessel's (1975) results for other ion line emission near the limb. These higher excitation temperatures (type 2 line source function of Figure 7) must decrease to a low value near 300 km, where the line source function is fixed by the deep cores of the disk profiles almost independently of all other parameters. The saturated cores are not very sensitive to the abundance, and also not to the micro- and macroturbulence because of the HFS-broadening. The steep outward decrease leads then to too narrow inner wings of the disk profiles.

Finally, narrow humps as in the type 3 line source functions (Figure 7) give proper emission wings. However, the microturbulent velocities needed to wash the hump out in the wings of the disk profiles are unacceptably high (≈ 5 km s^{-1} at 100 km). Moreover, the hump produces too shallow cores in the lines of multiplet 2, of which the line source functions will follow the hump at least partly because their metastable lower levels will be largely in collisional equilibrium with the ground level.

In these calculations the assumption of LTE in the ionization equilibrium was tested by entering arbitrary ionization temperatures into the Saha equation. After compensation of the barium abundance the net effect is a change of the shape of the contribution function. Large changes produced noticeable changes in the profiles, but attempts to fit all profiles simultaneously were not successful.

5. Calculations Based on Partial Redistribution

5.1. Formulation

The extensive analysis summarized in the previous section shows that simple one-dimensional frequency-independent line source functions cannot explain the formation of the emission wings of Ba II λ4554 near the limb simultaneously with the disk profiles. I then rejected the assumption of complete redistribution (CRD), inspired by the example of Vardavas and Cram (1974), who showed that the introduction of partial frequency redistribution (PRD) in the wings of the Ca II K line leads to a completely different source function for the K_1 feature.

For the much weaker Ba II λ4554 resonance line, PRD effects were not expected to be important on the disk because the part of the profile that is not redistributed by Doppler shifts ($\Delta\lambda \gtrsim 3\Delta\lambda_D$) is formed in deep layers where collisional damping is large, so that any frequency coherency will be destroyed. However, very close to the limb the wings are formed so high in the atmosphere that the collisional damping γ_{COLL} drops below the radiative damping γ_{RAD}. Indeed, for a line of sight at $h_0 = -1500$ km (where the emission wings start to appear), the optical depth at $\Delta\lambda = 0.1$Å ($\gtrsim 5\Delta\lambda_D$) is unity at -100 km, about the level where $\gamma_{RAD} = \gamma_{COLL}$. Effects of PRD are therefore to be expected for observations from $h_0 = -1500$ km outwards. These effects move progressively towards the line core, because for increasing height both temperature and microturbulence decrease, reducing the already small barium Doppler width substantially.

Thus, effects of PRD are expected in the formation of the λ4554 resonance wings near the solar limb, where indeed the emission wings occur. A problem is now encountered with our method of empirically fitting profiles from trial-and-error line source functions: the various population mechanisms must be known for a precise determination of the relative probability of resonance scattering throughout the profile and the atmosphere. In the absence of reliable kinetic equilibrium calculations, the empirical approach was maintained by specifying an

approximate wavelength-dependent line source function

$$S_\lambda^l(h) = (1-\alpha)S_0(h) + \alpha S_1(h) \tag{3}$$

with

$$\alpha(\lambda,h) = 1 - \exp\left[-\left|\frac{\Delta\lambda}{\sigma\Delta\lambda_D}\right|^\rho\right], \tag{4}$$

where S_0 is the line source function at line center and S_1 is the line source function for the wings. The parameters σ and ρ are fitting parameters that determine the extent of the Doppler redistribution by thermal and small-scale non-thermal motions, and the steepness of the transition between the two source functions. They are similar to the parameters employed by Vardavas and Cram (1974) in the scattering term of the Ca II K source function.

This simple approximation mimics the proper wavelength-dependence in having a Doppler-redistributed core and a steep transition to the partially coherent line source function in the wings. It fails in being asymptotically independent of wavelength in the far wings. However, in the λ4554 line these are formed so deep that collisional redistribution destroys the coherence; the use of a single source function in the wings seems a reasonable approximation. The wavelength- and height dependence of the mean intensity J, the scattering probability and the Zanstra factor $\gamma_{RAD}/(\gamma_{RAD}+\gamma_{COLL})$ result together in the shape of $S_1(h)$, to be determined empirically.

5.2. THE BEST-FIT MODEL FOR λ4554

Profiles of the λ4554 line from the disk and from the limb were calculated for a variety of frequency-dependent line source functions of the type given by Equation (3), using the VAL model. An extensive trial-and-error procedure as described in Section 4 yielded a 'best-fit model', defined by the excitation temperatures of Figure 8a. These are thickly drawn where they are best defined: the line cores over the disk are most sensitive to the S_0 core source function around 300 km, while the emission wings near the limb are sensitive to the S_1 wing source function in deeper layers. The CRD-PRD transition parameters of the best-fit model are $\sigma = 3$ and $\rho = 4$ respectively, and may range between $\sigma = 2.5 - 3.5$ and $\rho = 3 - 6$, in good agreement with the values of Vardavas and Cram (1974) for their similar parameters.

For a constant microturbulence of $1.5\ \mathrm{km\ s^{-1}}$ the excitation temperatures of Figure 8a produce the wavelength-dependent line source function of Figure 8b. The markings indicate the heights where $\tau_\lambda = 1$, respectively for disk center and for a line of sight near the limb with $h_0 = -500$ km (crosses). The latter line of sight is representative of the eclipse observations, while the Moon blocks no photosphere yet and the depth $\tau_\lambda = 1$ is still well defined (closer to the limb the contribution function widens rapidly, and the regions 'behind the limb' contribute also).

The profiles calculated with this line source function show an excellent fit to the eclipse profiles when homogeneously blurred (Figure 9b). The three profiles across

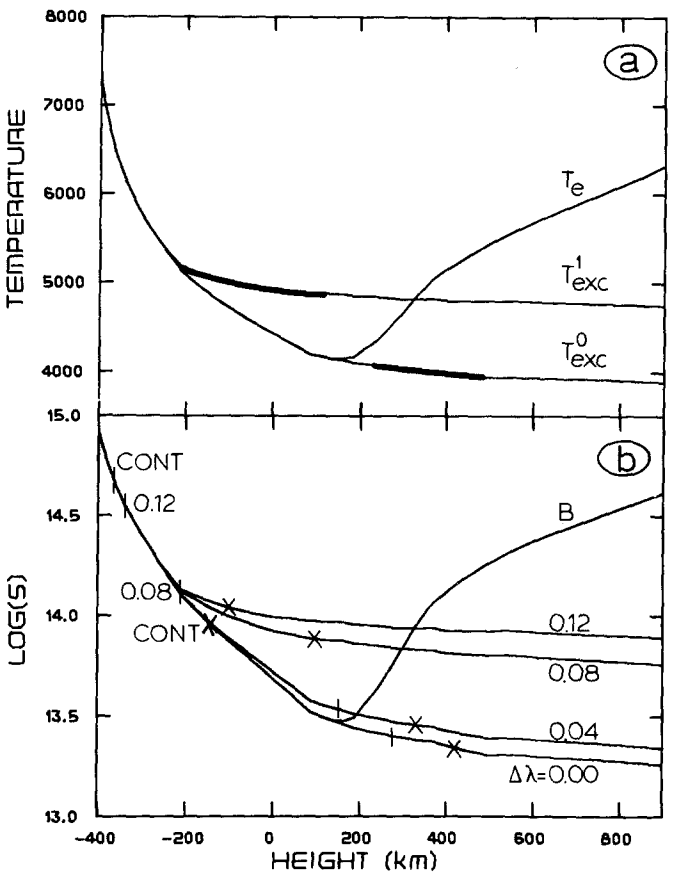

Fig. 8. The PRD line source function for λ4554 of the best-fit model. (a) Formal excitation temperatures for S_0 and S_1, thickly drawn where they are best determined in the empirical fitting procedure. (b) Wavelength-dependent line source function for a constant microturbulence of 1.5 km s^{-1}. The vertical tick marks and the crosses denote the heights where $\tau = 1$ in the best-fit model, for the indicated wavelength separations from line center and for lines of sight towards the solar center (*vertical ticks*) and near the limb with $h_0 = -500$ km (*crosses*).

the limb (Figure 11a) are also well produced in character (Figure 11c). For these the abundance was raised slightly to produce the little dip in the core at $h_0 = 0$ km and $h_0 = 200$ *km*, which increase is a plausible correction to the assumed LTE ionization to Ba III above 500 km. The good correspondence is in striking contrast with the complete dissimilarity of the CRD predictions (Figure 11b).

The empirically determined wing source function departs from B at the height where $\gamma_{RAD} \approx \gamma_{COLL}$. At the center of the disk the wings have $\tau_\lambda \ll 1$ at this height; for $\mu = 1$ there is no difference between profiles calculated with the wavelength-dependent line source function and profiles calculated with the core source function S_0 applied to the whole profile. But towards the limb the formation of the wings rises to these heights: for $\mu = 0.25$ and $\mu = 0.16$ there are differences of $\approx 10\%$ between such profiles, and neglect of the raised wing source function would lead to

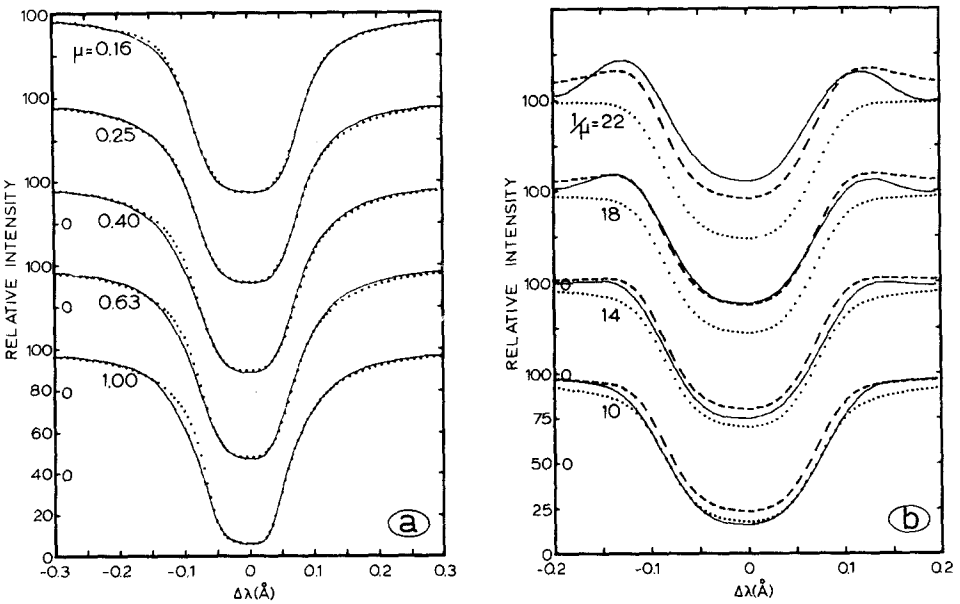

Fig. 9. Profiles of λ4554 for the best PRD fit. *Lines*: observed profiles. The computed profiles (*dots*) are the best-fit model: VAL atmosphere. NLTE-PRD line source functions of Figure 8b, $A = 2.5 \times 10^{-10}$, γ_6 = Deridder-Van Rensbergen, $v_{\text{macro}}^{\text{ver}} = 1.1$ km s^{-1}, $v_{\text{macro}}^{\text{hor}} = 2$ km s^{-1}. (a) Center-to-limb variation. Labelling as for Figure 6a. The microturbulence of Figure 10 was used. (b) Profiles near the limb. Labelling as for Figure 6a, with vertical offsets of 50%. *Microturbulence*: $v_{\text{micro}}^{\text{hor}} = 1.5$ km s^{-1}. *Dots*: no blurring (perfect seeing). *Dashes*: homogeneous blurring (worst seeing possible).

underestimation of the abundance and the horizontal component of the microturbulence (Rutten, 1976). For the line of sight with $h_0 = -1778$ km ($1/\mu = 14$) the calculated profile has raised wings, but not yet in emission (Figure 9b). It is the addition of radiation from larger heights that causes emission already for this line of sight. The assumption that the blurring is homogeneous represents an upper limit to this addition, so the derived wing source function is a lower limit.

An excellent fit to the disk profiles (Figure 9a) was obtained with the microturbulence of Figure 10. The profiles from the limb with this microturbulence fit the observations reasonably well (Rutten, 1976), though less than for the constant microturbulence (1.5 km s^{-1}) of Figure 9b. Their narrow cores imply a small horizontal component, whereas a steep outward increase fits the disk profiles better towards the limb: the hump in the horizontal component of Figure 10 represents a compromise. The low value above 400 km is quite significant, as is the anisotropy.

The *macroturbulence* determination is quite firm, because the HFS-splitting of the λ4554 line unexpectedly facilitates the separation of the microturbulence and the macroturbulence. For any microturbulence, the triple splitting pattern of Figure 2 is discernable in the line core unless macroturbulent smearing is applied. The value needed to smooth it into the observed asymmetrical, boxy core at disk center is sharply determined to 1.1 ± 0.1 km s^{-1}. Larger values make the core too

rounded. Towards the limb the fitting calculations gave 2.0 ± 0.2 km s^{-1}; the anisotropy in the macroturbulence is significant. These values apply to the layers just above the temperature minimum.

The value for the *barium abundance* of the best-fit model ($A = 2.5 \times 10^{-10}$, or $\log \varepsilon_{Ba} = 2.40$) was determined primarily from the wings. The saturated cores of the $\lambda 4554$ profiles are not very sensitive to the abundance, except that for $A \lesssim 1 \times 10^{-10}$ the boxy HFS pattern is not filled out properly. In the wings the usual ambiguity between the parameters in the product $fA\gamma$ is present. The Deridder-Van Rensbergen damping constant and the oscillator strength of Miles and Wiese (Section 2) were used, but none of these parameters could be determined to better than 30%.

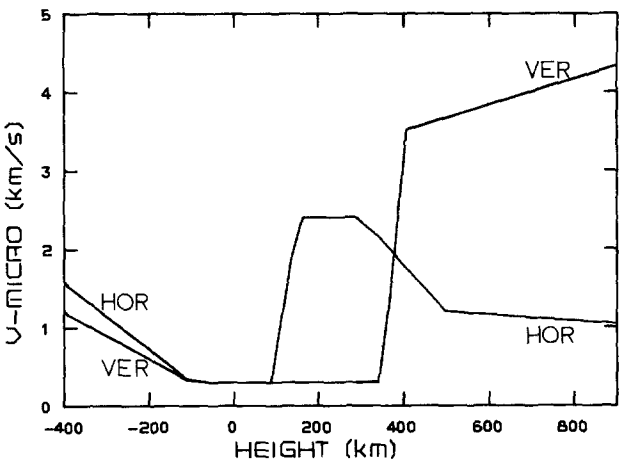

Fig. 10. The best-fit microturbulence model for the disk profiles. The vertical and horizontal components are indicated.

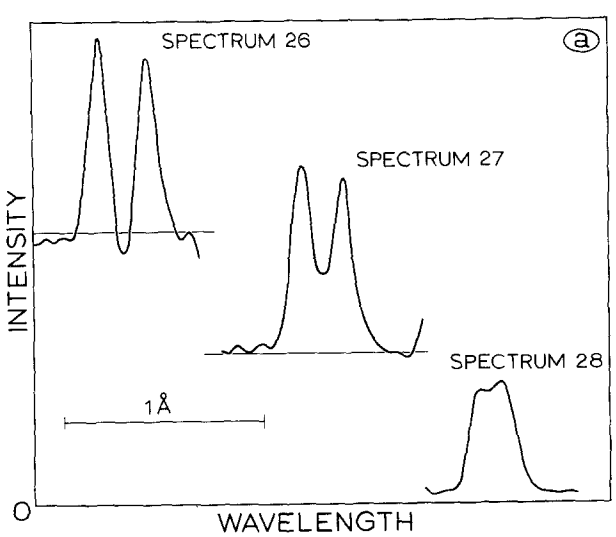

Fig. 11a.

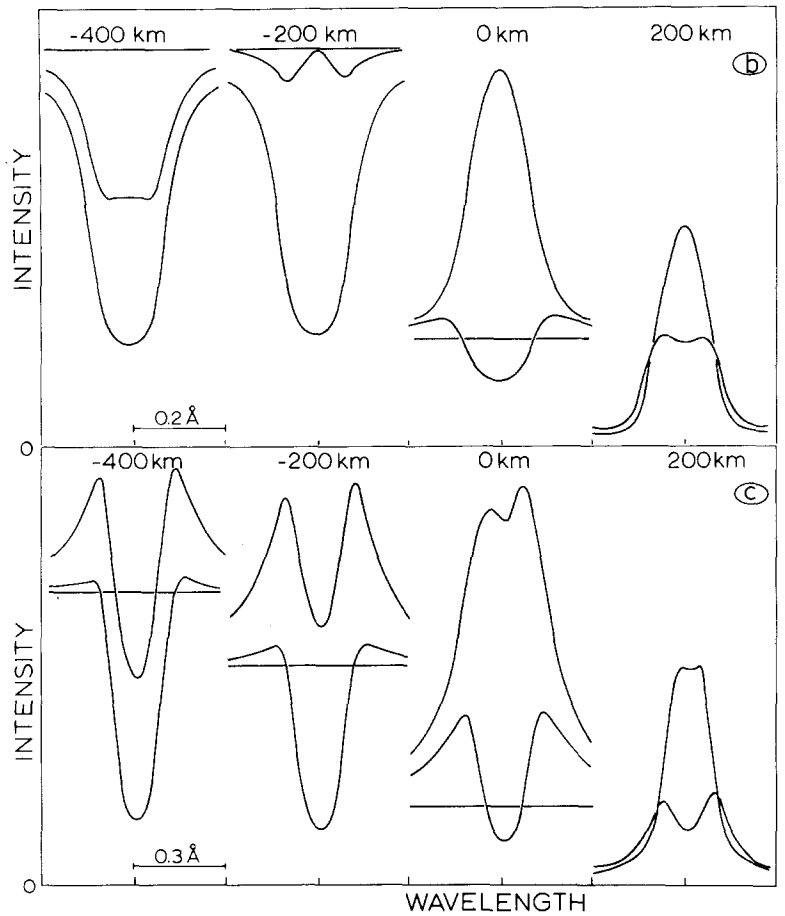

Fig. 11b.

Fig. 11a–b. Profiles of λ4554 at and above the limb. The relative intensity scale differs per profile (zero intensity common); the continua are indicated. (a) Observed profiles taken from Rutten (1977). The heights of the lunar limb at the beginning and end of the exposures were respectively: spectrum 26: −580, −290 km; spectrum 27: −230, +60 km; spectrum 28: +130, 2530 km. (b) Computed profiles for the best CRD fit (cf. Figure 6). *Lower profiles*: no blurring; *upper profiles*: homogeneous blurring. (c) Computed profiles for the best PRD fit (best-fit model of Figure 9) but with $A = 3 \times 10^{-10}$; $v_{\text{micro}}^{\text{hor}} = 1.5\ \text{km s}^{-1}$. *Lower profiles*: no blurring; *upper profiles*: homogeneous blurring.

5.3. Comparison with other data

The best-fit model for the λ4554 line was tested on the *other Ba II lines* of Table I. Their profiles were calculated and fitted by adjusting only the damping multiplication factor and the macroturbulence. Reasonable fits were obtained for the lines of multiplet 2.

The empirical *gf*-values of Table I and the abundance value of the best-fit model were used. The damping multiplication factors are 2, 1.7 and 3 for λ6142, λ6497 and λ5854 respectively. The macroturbulence values are: $v_{\text{macro}}^{\text{ver}} = 1.1$, $v_{\text{macro}}^{\text{hor}} = 2.0\ \text{km s}^{-1}$ for λ6142 (as for λ4554) and $v_{\text{macro}}^{\text{ver}} = v_{\text{macro}}^{\text{hor}} = 1$ and $1.5\ \text{km s}^{-1}$ for

λ 6497 and λ 5854 respectively. There was no difference between profiles calculated with the best-fit model's PRD line source function or a CRD variation (the S_0 core source function of Figure 9 applied to the whole profile), except for the strong λ 6142 line. The PRD fit of this line is better than the CRD fit. More details may be found in Rutten (1976).

No good fit was found for the weak λ 4131 line. Its upper level population is unknown, while its lower level is formed out of LTE already deep in the atmosphere due to the NLTE source function of the λ 4554 PRD wings. In classical analyses, however, this weak line would be expected to be formed in LTE. This line had extra weight in Holweger and Müller's (1974) determination of the barium abundance because it is hardly sensitive to the collisional damping. Figure 12 shows the Holweger-Müller disk-center fit and its extension towards the limb. The fit is poor away from disk center. It was improved by adjusting the macroturbulence, which procedure is representative of changing the total turbulence for this weak

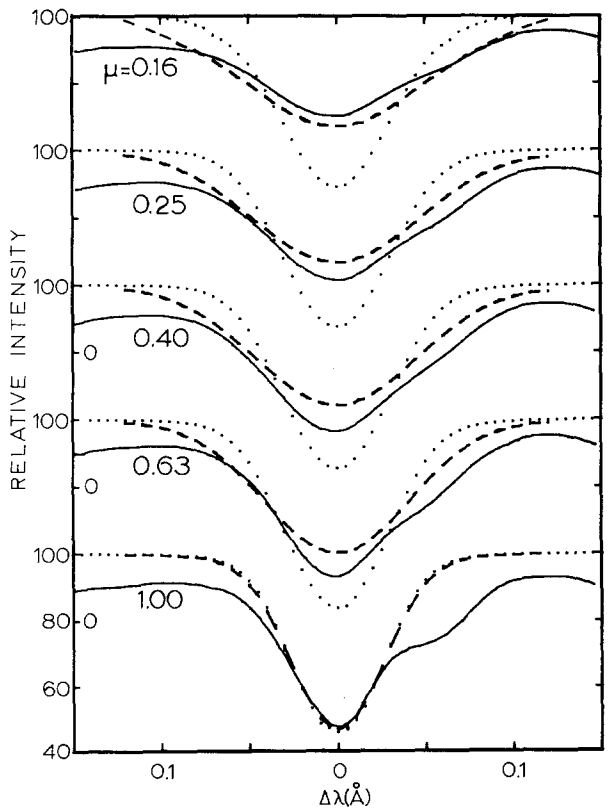

Fig. 12. Center-to-limb variation of the λ 4131 line. Labelling as for Figure 6a. *Lines*: observed profiles. The computed profiles are for the Holweger-Müller disk-center fit: Holweger-Müller atmosphere, LTE, $A = 1.3 \times 10^{-10}$, $\gamma_6 = 3 \times$ Van der Waals, microturbulence of Garz *et al.* (1969) but with the ultimate value replaced by 0.5 km s^{-1}, $v_{\text{macro}}^{\text{ver}} = 1.6$ km s^{-1} and two horizontal macroturbulence components: $v_{\text{macro}}^{\text{hor}} = 1.6$ km s^{-1} (*dots*) and $v_{\text{macro}}^{\text{ver}} = 4.2$ km s^{-1} (*dashed*).

line. The profile at $\mu = 0.2$ can be fitted with a large increase of the horizontal macroturbulence (Figure 12), but then the calculated profiles are too shallow at the intermediate positions. Appreciable adjustment of the line source function is therefore necessary. Thus, the λ4131 line shows deviations from LTE, to a larger extent than the differences between the VAL model and the Holweger-Müller model furnish. Valuable constraints are provided by the inclusion of profiles from intermediate disk positions also in abundance analyses.

Finally, *chromospheric intensities* were calculated for the five Ba II lines observed by Dunn *et al.* (1968), who specify line lengths integrated over wavelength as well as over the height of yet uncovered chromosphere, for a range of lunar limb positions above $h_0 = 100$ km. For all observed Ba II lines these values are considerably higher above $h_0 = 300$ km than the values computed by similar integrations from the best-fit model. This discrepancy (up to a factor 4 for λ4554) remains even when the assumed LTE ionization equilibrium is changed so that barium remains singly ionized at all heights. This is unlikely, and in fact extra ionization to Ba III is to be expected because the ionization energy from the Ba II ground level equals the radiative energy in the PRD-wing of Lα, which is formed at these heights (Barium is the only element with a second ionization potential below the Lα excitation potential).

Subsequent calculations with arbitrary upper level departure coefficients showed that with steep increases above $h \approx 1000$ km these high chromospheric intensities can be reproduced. They cannot occur much lower in the chromosphere because then the cores of the profiles over the disk and near the limb are too much affected. Tandberg-Hanssen (1964) derived similar steep increases for the 6P populations from statistical equilibrium calculations for temperatures and densities quite different from the Val model.

Similar difficulties to reproduce the high values of the Dunn *et al.* (1968) emission strengths of various Ti II lines from the disk source functions of Pecker and Pottasch (1969) were experienced by Groeneveld (1974), who suggested that either errors in the photometric calibration or the presence of inhomogeneities cause this discrepancy. The results of Tanaka (1971a), based on independent observations, also indicate that inhomogeneity is the major aspect of the chromospheric spectrum above $h \approx 500$ km.

6. Discussion

6.1. The line source function of λ4554

The best-fit model presented in the previous section reproduces the observed λ4554 profiles satisfactorily, both over the disk and at the extreme limb; it is compatible with the other Ba II lines. Effects of NLTE and PRD are essential elements of this interpretation, in contrast to the analysis by Holweger and Müller (1974). Various processes may contribute to increase the complexity of line forma-

tion even further: increased rugosity near the limb (i.e. the projection effects of inhomogeneous structure; cf. Redman, 1943), the increase of inhomogeneity with height towards the chromosphere, and anisotropic scattering near the limb. The inhomogeneities are taken at least partly into account with the turbulent smearing parameters, in which the rugosity enters as (extra) height and angle dependence. Although a multi-component model may in principle explain the emission wings observed near the limb *without* PRD effects, it will be difficult to reconcile its necessarily large effects in layers well below the temperature minimum with the disk profiles and the line cores near the limb. Prime importance has been given to the effects of *frequency* redistribution because the PRD effects *have* to be present near the limb where the wings are formed with $\gamma_{\mathrm{RAD}} > \gamma_{\mathrm{COLL}}$. They produce changes especially in the wings, and in still deep layers.

Above the temperature minimum, the inconsistency of the chromospheric Ba II emission line strengths with the photospheric line source functions indicates that the one-dimensional approach fails as a first approximation. This is in agreement with Tanaka's (1971a, b) conclusions and also with Canfield and Stencel's (1977) demonstration that the emission lines in H and K, formed near the temperature minimum, show no fine structure except when they are interlocked to strong chromospheric lines.

The results given here demonstrate the need for kinetic equilibrium calculations in a model barium atom. These will be hampered by the poor atomic data available, the hyperfine structure, by the necessity to incorporate the connected transitions to the metastable 6D levels which have coherency effects of their own, and by the anisotropy of the Doppler width near the limb, of which the influence on the redistribution cannot be specified when the cause of the anisotropy is not better known. A first step to such calculations has become available with the generalization of the complete linearization method to include PRD in the presence of connected metastable levels by Milkey *et al.* (1975). Their application to the Ca II K line (Shine *et al.*, 1975) confirmed and extended the results of Vardavas and Cram (1974).

Although the best-fit model represents only a first approximation to the formation of the $\lambda 4554$ line, its basic structure (Figure 8) is well determined. Its essential elements are the discrete high wing source function below the temperature minimum, and the slowly decreasing low core source function at and above the minimum. While this structure was found in a completely empirical manner, it is well understandable. The *core source function* shows the same behaviour as the Ca II K line source function at the location of the K_1 dip (Shine *et al.*, 1975). Since K_1 is outside the Doppler-redistributed K-line core, the K_1 line photons represent an ensemble independent of the rest of the K line, comparable to the similar independent ensemble of $\lambda 4554$ core photons, because the line absorption coefficient decreases from K_3 to K_1 over the Ca/Ba abundance ratio (10^4) and both lines are similarly formed by scattering. The rest intensities of K_1 and the core of $\lambda 4554$ are indeed about equal.

The *wing source function* departs from B at the height where $\lambda_{\mathrm{RAD}} \approx \lambda_{\mathrm{COLL}}$. Above this height PRD effects are possible; they become pronounced for lines of sight that give a total optical depth of unity or larger above this height outside the Doppler-redistributed core. This is the case for $h_0 \geqslant -1500$ km. The important aspect of PRD in λ4554 is that the independent line wing, uncoupled from the core, assumes the character of a *weak* line. The *monochromatic* mean intensity J_ν enters in the scattering contribution to the line source function instead of the profile-averaged mean intensity $\int J_\nu \phi_\nu \, d\lambda$. In the narrow λ4554 line J_ν is large already at 4 or 5 Doppler widths from line center, and J rises substantially above the continuum source function B in higher layers due to the steep gradient of $B(h)$ in the blue (cf. Vernazza *et al.*, 1976, Figure 23). Thus, the weakness of the λ4554 wings, the importance of scattering, and the steep gradient of $B_\nu(h)$ contributing to the wings combine to a large wing source function in high layers, independently of the non-weak character of the line core.

The λ4554 emission wings are therefore similar in origin to the weak limb emission lines of Ce II outside H and K (Canfield, 1969, 1971) and to the weak ion lines in the violet discussed by Tanaka (Tanaka, 1971a, b), whose 'fishbone' line source function structure is here exhibited *within* the λ4554 source function.

The similarity of the Ba II λ4554 resonance line to the Ca II K line extends not only to their atomic level structure, but also to the presence of effects of PRD in their formation. The large abundance ratio ($\mathrm{Ca/Ba} \approx 10^4$) results in quite different manifestations of these. While in the strong H and K lines it is the location of the CRD-PRD core-wing transition above the temperature minimum which leads to pronounced line structure, in λ4554 it is the weakness of the PRD wings that results in observable emission *within* the limb.

6.2. Turbulence, inhomogeneities

The microturbulence and macroturbulence of the best-fit model are both height and angle dependent. Since they measure the solar velocity fields and inhomogeneities (including rugosity) at all scales, these dependencies are not surprising: all resolvable components (granulation, oscillations) vary with height and angle. Clearly the classical turbulences are not a physically correct description of these effects (cf. Rutten *et al.*, 1974). Here, the turbulences have served as final fitting parameters, chiefly to demonstrate that the observations can be reproduced. The details of the microturbulence model, as the hump in the horizontal component (Figure 10), should therefore be regarded as fitting peculiarities that also contain the errors of the model, for instance in the atmosphere and in the representation of the distribution effects. The coupling of the anisotropy of the inhomogeneities with the line source function will be more complicated than the simple Doppler width relation of Equation (4). Still, the empirical microturbulence of Figure 10 conforms roughly to the usual pattern (Canfield and Beckers, 1975): anisotropy and a minimum near the temperature minimum. The anisotropy of both the microturbulence and the macroturbulence above the minimum are significant.

The flash intensities above 500 km of Dunn *et al.* (1968) are so large that inhomogeneities must be a prime aspect of their explanation (Section 5).

6.3. λ4554 ASYMMETRY

The blue-wing depression of the λ4554 line at disk center is largest where the profile is most sensitive to PRD effects. This suggests PRD-enhancement of the sensitivity of the profile to systematic motions: coherently scattering wing photons may be blocked by Doppler shift in high layers rather than escape freely (cf. Vardavas and Cram, 1974). Such enhancement may explain that the λ4554 line is the only one in the solar sample of Smith and Parsons (1976) that shows an asymmetry similar to the blue-wing depressions observed in stellar lines.

The asymmetry observed in the emission peaks of the line at the limb (Figure 11a, spectrograms 26 and 27) is also of interest. The observed blue peak is larger – similar to the averaged Ca II K_2 peaks and the Mg II h_2 and k_2 peaks, which originate at about the same height in the atmosphere. This asymmetry may again reflect enhanced sensitivity to differential motions, through Doppler trapping of scattering photons followed by re-emission towards the observer. The profile from the last eclipse spectrogram (Figure 11a, nr. 28) shows a higher *red* peak, in agreement with the calculated profile (Figure 11c). The peaks of this profile lie within the range of Doppler redistribution and apparently show the asymmetry due to the hyperfine structure only.

6.4. BARIUM ABUNDANCE

The increased complexity of the λ4554 formation leads to increased uncertainty of the barium abundance value. The abundance value found here with the Deridder and Van Rensbergen (1974) collisional damping constant ($\log \varepsilon_{\mathrm{Ba}}^{\mathrm{SUN}} = 2.40$) is twice the LTE value of Holweger and Müller (1974). The difference seems a good representation of the uncertainty range, to which the approximations in the PRD line source function and in the ionization equilibrium contribute. The meteoritic abundance value ($\log \varepsilon = 2.32$, cf. Holweger and Müller 1974) is contained in this range.

Holweger and Müller's conclusion that the solar isotope ratios of barium equal the terrestrial values is confirmed, in the sense that the ratio (Ba 135 + Ba 137)/(Ba 134 + Ba 136 + Ba 138) agrees. No further distinction is possible because the odd isotopes contribute equally to the λ4554 splitting pattern (Figure 2).

6.5. ATMOSPHERIC MODEL

The uncertainties in the best-fit model do not warrant a reliable test of different atmospheric models with the Ba II data. Calculations were performed also with the HSRA model (Gingerich *et al.*, 1971), for which similar fits can be obtained with slight changes of the other parameters. Reversely, the differences between the

VAL and the HSRA models are small compared to the effects analysed here, so that the main conclusions are not affected by model uncertainties.

Acknowledgements

I thank L. E. Cram, A. G. Hearn, H. Holweger, R. A. Shine, I. M. Vardavas and in particular C. Zwaan, who suggested and guided this analysis, for valuable comments and discussions. I am indebted to H. Nieuwenhuijzen, L. Neven and L. Testerman for the disk observations. Kitt Peak National Observatory is operated by the Association of Universities for Research in Astronomy, Inc. under contract with the National Science Foundation.

The eclipse expedition which yielded the valuable extreme limb data was supported by the Netherlands Organization for the Advancement of Pure Research (ZWO). The expedition was proposed and led by J. Houtgast.

References

Athay, R. G.: 1972, *Radiation Transport in Spectral Lines*, Dordrecht, D. Reidel Publishing Company.
Bidelman, W. P. and Keenan, Ph. C.: 1951, *Astrophys. J.* **114**, 473.
Brix, F. and Kopfermann, H.: 1952, Landolt-Börnstein, I/5, Berlin, Springer.
Burbidge, E. M. and Burbidge, G. R.: 1957, *Astrophys. J.* **126**, 357.
Candler, C.: 1964, *Atomic Spectra*, London, Hilger and Watts.
Canfield, R. C.: 1969, *Astrophys. J.* **157**, 425.
Canfield, R. C.: 1971, *Astron. Astrophys.* **10**, 64.
Canfield, R. C. and Beckers, J. M.: 1976, in R. Cayrel and M. Steinberg (eds.), *Physique des mouvements dans les atmosphères stellaires*, Colloques Internationaux du CNRS No. 250.
Canfield, R. C. and Stencel, R.: 1976, *Astrophys. J.* **209**, 618.
Deridder, Gh. and Van Rensbergen, W.: 1974, *Solar Phys.* **34**, 77.
Deridder, Gh. and Van Rensbergen, W.: 1976, *Astron. Astrophys. Suppl.* **23**, 147.
Dunn, R. B., Evans, J. W., Jefferies, J. T., Orrall, F. Q., White, O. R., and Zirker, J. B.: 1968, *Astrophys. J. Suppl.* **15**, 275.
Evans, J. C. and Testerman, L. K.: 1975, *Solar Phys.* **45**, 41.
Garz, T., Holweger, H., Keck, M., and Richter, J.: 1969, *Astron. Astrophys.* **2**, 466.
Gingerich, O., Noyes, R. W., Kalkofen, W., and Cuny, Y.: 1971, *Solar Phys.* **18**, 347.
Goldberg, L., Müller, E. A., and Aller, L. H.: 1960, *Astrophys. J. Suppl.* **5**, 1.
Groeneveld, R.: 1974, Ph.D. Thesis, University of Groningen.
Holweger, H.: 1967, *Z. Astrophys.* **65**, 365.
Holweger, H. and Müller, E A.: 1974, *Solar Phys.* **39**, 19.
Houtgast, J., Namba, O. and Rutten, R. J.: 1976, *Proc. Kon. Ned. Akad. Wetensch. Amsterdam, Series B*, **79**, 221.
Kopfermann, H.: 1956, *Kernmomente*, Frankfurt.
Kurucz, R. L. and Peytremann, E.: 1975, *A Table of Semiempirical gf Values*, Smithsonian Astrophysical Observatory, Special Report 362.
Landi Degl'Innocenti, E.: 1976, *Astron. Astrophys. Suppl.* **25**, 379.
Lambert, D. L. and Warner, B.: 1968, *Monthly Notices Roy. Astron. Soc.* **140**, 197.
Magnan, C. and Pecker, J.-C.: 1974, in Contopoulos (ed.), *Highlights of Astronomy* **3**, 171.
Miles, B. M. and Wiese, W. L.: 1969, *Atomic Data* **1**, 1.
Milkey, R. W., Shine, R. A., and Mihalas, D.: 1975, *Astrophys. J.* **199**, 718.
Minnaert, M. G. J.: 1935, *Z. Astrophys.* **10**, 40.

Noyes, R. W.: 1967, in R. N. Thomas (ed.), *Aerodynamic Phenomena in Stellar Atmospheres*, London , Acad. Press, p. 293.
Pecker, J.-C. and Pottasch, S. R.: 1969, *Astron. Astrophys.* **2**, 81.
Redman, R. O.: 1943, *Monthly Notices Roy. Astron. Soc.* **103**, 173.
Rutten, R. J.: 1976, Ph.D. Thesis, University of Utrecht, Utrecht Astronomical Reprint Series No. 365.
Rutten, R. J.: 1977, *Solar Phys.* **51**, 3.
Rutten, R. J., Hoyng, P., and De Jager, C.: 1974, *Solar Phys.* **38**, 321.
Shine, R. A., Milkey, R. W., and Mihalas, D.: 1975, *Astrophys. J.* **199**, 724.
Smith, M. A. and Parsons, S. B.: 1975, *Astrophys. J. Suppl.* **29**, 341.
Smith, M. A. and Parsons, S. B.: 1976, *Astrophys. J.* **205**, 430.
Tanaka, K.: 1971a, *Publ. Astron. Soc. Japan* **23**, 185.
Tanaka, K.: 1971b, *Publ. Astron. Soc. Japan* **23**, 217.
Tandberg-Hanssen, E.: 1964, *Astrophys. J. Suppl.* **9**, 207.
Tandberg-Hanssen, E. and Smythe, C.: 1970, *Astrophys. J.* **161**, 289.
Unsöld, A.: 1955, *Physik der Sternatmosphären*, Berlin, Springer Verlag.
Van Dessel, E. L.: 1975, *Solar Phys.* **44**, 13.
Van Rensbergen, W.: 1970, *Solar Phys.* **11**, 11.
Van Rensbergen, W., De Doncker, E., and Deridder, Gh.: 1975, *Solar Phys.* **40**, 303.
Vardavas, I. M. and Cram, L. E.: 1974, *Solar Phys.* **38**, 367.
Vernazza, J. E., Avrett, E. H., and Loeser, R.: 1976, *Astrophys. J. Suppl.* **30**, 1.
Warner, B.: 1965, *Monthly Notices Roy. Astron. Soc.* **129**, 263.
Wijbenga, J. W. and Zwaan, C.: 1972, *Solar Phys.* **23**, 265.